Walter, T. R., Salzer, J. T., Varley, N., Navarro, C., Arámbula-Mendoza, R., Vargas-Bracamontes, D. (2018): Localized and distributed erosion triggered by the 2015 Hurricane Patricia investigated by repeated drone surveys and time lapse cameras at Volcán de Colima, Mexico. - *Geomorphology*, *319*, pp. 186—198.

DOI: http://doi.org/10.1016/j.geomorph.2018.07.020

Geomorphology 319 (2018) 186–198

Contents lists available at ScienceDirect

Geomorphology

journal homepage: www.elsevier.com/locate/geomorph

Localized and distributed erosion triggered by the 2015 Hurricane Patricia investigated by repeated drone surveys and time lapse cameras at Volcán de Colima, Mexico

Thomas R. Walter [a,*], Jacqueline Salzer [a], Nick Varley [b], Carlos Navarro [c], Raul Arámbula-Mendoza [c], Dulce Vargas-Bracamontes [c,d]

[a] GFZ German Research Centre for Geosciences, Telegrafenberg, 14473 Potsdam, Germany
[b] Facultad de Ciencias, Universidad de Colima, Av. Bernal Díaz del Castillo #340, Col. Villas San Sebastián, C.P. 28045 Colima, Mexico
[c] Centro Universitario de Estudios e Investigaciones Vulcanológicas (CUEIV), Universidad de Colima, Av. Bernal Díaz del Castillo #340, Col. Villas San Sebastián, C.P. 28045 Colima, Mexico
[d] CONACYT-CUEIV, Universidad de Colima, Av. Bernal Díaz del Castillo #340, Col. Villas San Sebastián, C.P. 28045 Colima, Mexico

ARTICLE INFO

Article history:
Received 23 March 2018
Received in revised form 12 June 2018
Accepted 23 July 2018
Available online 24 July 2018

Keywords:
Volcano hazard
Volcán de Colima
Erosion
Lahar deposits
Rainfall triggering
Photogrammetry
Drones

ABSTRACT

In October 2015, Patricia, a major category 5 hurricane, made landfall in western Mexico, resulting in 500 mm cumulated rainfall and lahar generation along the southerly directed Montegrande valley of Volcán de Colima. We monitored lahar deposition and erosion using time-lapse trail cameras and conducted repeated camera drone overflights, two days before and after the hurricane. Using photogrammetric processing we derive a unique dataset of high resolution digital terrain models and study the geomorphologic impacts of a single lahar event. Results reveal different types of erosion at 8 km distance from the volcano, with overland flow and rill networks, developing into major erosion gullies exceeding a depth of 4 m, as well as bank collapse, oversteepening and marginal erosion. We find alternating deposition and erosion zones that depend on general slope and valley width, and find that the overland flow related erosion is an important contributor to the bulking process of lahars. Moreover, this study shows that camera monitoring is very useful for studying the relationship between volcano landscape evolution and hydrometeorological extremes and for rapid assessment associated with single lahar events.

1. Introduction

At the summit regions of explosive volcanoes, the accumulation of rainwater and the resulting mobilization of clastic material downslope often lead to lahars, which are a major secondary volcanic hazard (Naranjo et al., 1986; Pierson and Costa, 1987). Lahars pose a threat to people and infrastructure both during their deposition, through processes such as burial, scouring, removal and trapping during lahar inundation (Leung et al., 2003; Vallance and Iverson, 2015), as well as afterwards, as the soft lahar deposits may amplify sagging, liquefaction or shaking site effects during earthquakes (Walter et al., 2008).

Lahars form different types of flows, where the relative proportions of water, sediment and coarser debris may greatly vary and form flows of different characteristics, such as debris flows and hyperconcentrated flows (Vallance, 2000). Common understanding is that lahars begin as erosive water flows entraining unconsolidated material, changing into a sediment-laden hyperconcentrated flow with a sediment fraction of about 20–60% (Beverage and Culbertson, 1964) or even exceeding 60% by volume (Pierson and Costa, 1987). The entrainment of sediments and water leads to an increase of the volume of a lahar ("bulking"), details of which are commonly difficult to decipher in the field (Procter et al., 2010) but are understood that they may increase the volumes by three to five times of initial flow and may generate lahar hazards hundreds of kilometres away (Pierson and Costa, 1987; Cronin et al., 1997). During transport, lahars may deposit sediments several metres thick with complicated internal structure (Gomez et al., 2018) that in some cases are quickly eroded again within short time spans of weeks to months (Lavigne et al., 2000). While most earlier studies mainly concentrate on lahar mobility and deposition, the type and scale of erosion and associated morphology change remains less investigated. To best investigate erosion processes and to reduce artifacts arising from later redepositing and infilling, studies related to lahar erosion structures therefore need to be realized very soon after their occurrence, as long term preservation of unconsolidated sedimentary structures is often unlikely. Here we present the results of repeat morphology measurements performed using low-cost drone based photogrammetry surveys shortly before and after the occurrence of a lahar. We demonstrate the potential of such techniques for studying lahar deposition and erosion, in particular at those volcanoes where lahars are very common.

* Corresponding author.
E-mail address: twalter@gfz-potsdam.de (T.R. Walter).

https://doi.org/10.1016/j.geomorph.2018.07.020

1.1. Lahars and morphology change

Morphology change associated with lahars is often highly complex, with variations between erosion and deposition. Studies at Ruapehu volcano, New Zealand, showed that erosion and deposition alternate downstream, and may closely relate to the valley morphology, particularly its slope and width (Procter et al., 2010). The details of erosion processes in the literature are commonly limited to channel erosion descriptions, which may be the result of a limitation that arises from the low resolution of the available data. However, consulting the literature addressing soil erodibility and water erosion at non-volcanic regions (Bryan, 2000), we may find a wide spectrum of erosion forms that could similarly be investigated associated with lahar events produced at volcanoes.

Previous lahar morphology studies have compared digital elevation models to study erosion and sedimentation, e.g. using topographic contour maps with a few tens of metres resolution (Jones and Newhall, 1996). Satellite radar (Solikhin et al., 2015) and tri-stereo optical data (Poli et al., 2015) have greatly enhanced resolution and thus contributed to the identification of geomorphological changes associated with lahar events. With new photogrammetric technologies, such as structure-from-motion (SfM), cost effective and high resolution morphology studies (Westoby et al., 2012) now become even more feasible in steep volcanic terrains (James and Varley, 2012) with improved precision (James and Robson, 2014). Major drainages can be accurately identified by such data, and small scale changes become visible. Studies using high resolution LiDAR data have allowed the comparison of the topography from two surveys realized some months or years apart, and are leading to improved process understanding (Procter et al., 2010), however, as this data is very costly, individual events remain hardly distinguishable.

Comparison of digital elevation models prior to and following lahar events is allowing the identification of a sinusoidal alternating recurrence of deposition-erosion over kilometres distance (Procter et al., 2010), highlighting the complexity of lahar bulking. Rill erosion with small dimensions (Shen et al., 2015) at lahars has remained largely unstudied, however, even though their influence on lahar bulking processes appears plausible. As we show here, by use of modern drone based and time lapse camera data, we can (i) monitor morphologic changes associated with a single lahar event, and (ii) retrieve spatial resolutions that allow deciphering even small scale geomorphologic changes, results of which potentially allow an improved understanding of the underlying processes leading to morphological changes.

In general, the source region of sediment-laden lahars is commonly located on the higher slopes of a volcano, while deposition occur further downslope (Vallance, 2000). This is associated with the higher rainfall in mountainous regions, and higher erosion capacity of turbulent and energetic water-rich lahars if compared to sediment-rich lahars further downslope (Vallance and Iverson, 2015). In certain cases, lahars that occur during an extreme rainfall, however, may differ from this typical scenario, as there is high bulking and erosional capacity also at larger distances from the volcano, due to a constantly high water volume addition within lower regions. This can lead to a more complex development of the lahar with distance from the source.

Even though lahars at volcanoes are common during typical or above average rainfall (Dávila et al., 2007; Vázquez et al., 2016), hurricane-rainfalls and associated single lahar events are rarely investigated in detail (Scott et al., 2005). Here we provide evidence for deep erosion and sediment remobilization by a single lahar event at 8 km distance to the volcano summit at Volcán de Colima, Mexico, an area which was close to the eye of the largest ever recorded Hurricane in the Western Hemisphere: the October 2015 Hurricane Patricia.

1.2. Study area

Volcán de Colima (elevation 3855 m above sea level) is located in the western part of the Trans-Mexican volcanic belt and shows complex volcano-tectonic interactions (Escudero and Bandy, 2017; Spica et al., 2017), and is the site of documented major Plinian eruptions (Macías et al., 2017). The occurrence of lahars is prevalent during, but not limited to, the rainy season (commonly June–October), especially during rainfall events associated with tropical storms, which drain along the ravines that have directions to the SW, S and SE (Dávila et al., 2007; Vázquez et al., 2014), while the N of the volcano features the higher altitude mass of Nevado de Colima (Fig. 1).

The main directions of mass movements has varied with time, being more pronounced towards the west until 2015 (Hutchison et al., 2013; Walter et al., 2013; Salzer et al., 2017), and then changing to a southerly direction along the Montegrande ravine (Capra et al., 2016; Reyes-Dávila et al., 2016). Activity in 2015 included rapid dome growth, followed by its collapse with parts of the upper edifice forming an open amphitheatre, and the accumulation of $>4.5 \times 10^6$ m^3 deposits in the Montegrande ravine alone (Capra et al., 2016) in the form of block and ash flows. The Montegrande ravine represents one of the most important drainages and hence is prone to the formation of lahars, with both erosion and depositional processes (Vázquez et al., 2016).

In 2015, the conditions for lahar formation at Volcán de Colima and especially the Montegrande ravine were pervasive: after deposition of major volumes of unconsolidated sediments during the 7/2015 eruption (Capra et al., 2016; Reyes-Dávila et al., 2016; Capra et al., 2018b), the area was hit just three months later by an unprecedented category 5 hurricane in October 2015, leading to intense tropical-storm rainfalls at Volcán de Colima.

In this work we analyse erosional features associated with the lahar in the Montegrande ravine, which was also monitored by rain gauges and seismic stations (Fig. 2). We first describe briefly the precipitation events that critically increased the potential lahar hazards on the volcano slopes. The main study is then discussed based on close range photography datasets, using fixed time lapse cameras and multicopter unmanned aerial vehicles - UAVs (Fig. 1b). UAV overflights could be carried out just two days before and again repeated two days after the hurricane, providing a unique account of the various erosion features caused by a single rain/lahar event. Results reveal not only localized and channelized erosion alternating with deposition at ~8 km from the volcano summit, but also widespread overland flow and rill erosion. This study demonstrates the wide and flexible use of photogrammetric data and the potential for UAV supported monitoring strategies in lahar-prone areas.

2. Data and methods

2.1. Rainfall and seismic monitoring

The amount of rainfall was recorded every 15 min by a CNA (Comisión Nacional de Agua) meteorological station on the southern slopes of Volcán de Colima at Montitlán, located about 3.5 km to the SSW of the area herein studied in detail within the Montegrande ravine ("MET" in Fig. 1a). We note that the amount of rain shown here is likely lower than the rainfall that accumulated at higher elevations, therefore numbers discussed here are conservative, but relevant for understanding local overland flow erosion at a distance from the volcano.

The occurrence of lahars at Volcán de Colima is closely monitored by RESCO, the regional seismic monitoring network (Vázquez et al., 2016) that already previously has identified lahars (Zobin et al., 2009) and identified distinct lahar pulses (Vázquez et al., 2014). Distinct frequency components have been identified from the seismic waveforms, these being characteristic of lahars. Different stations are used for detecting lahars in various ravines. Data was considered from the seismic station located closest to the Montegrande ravine (MNGR, see Fig. 1a) and 5.3 km from the crater. It is a broadband Guralp CMG-6TD sensor with a flat response between 0.033 and 50 Hz. The sampling rate is of 100 Hz and the signal is transmitted via radio to the University of Colima in the city of Colima.

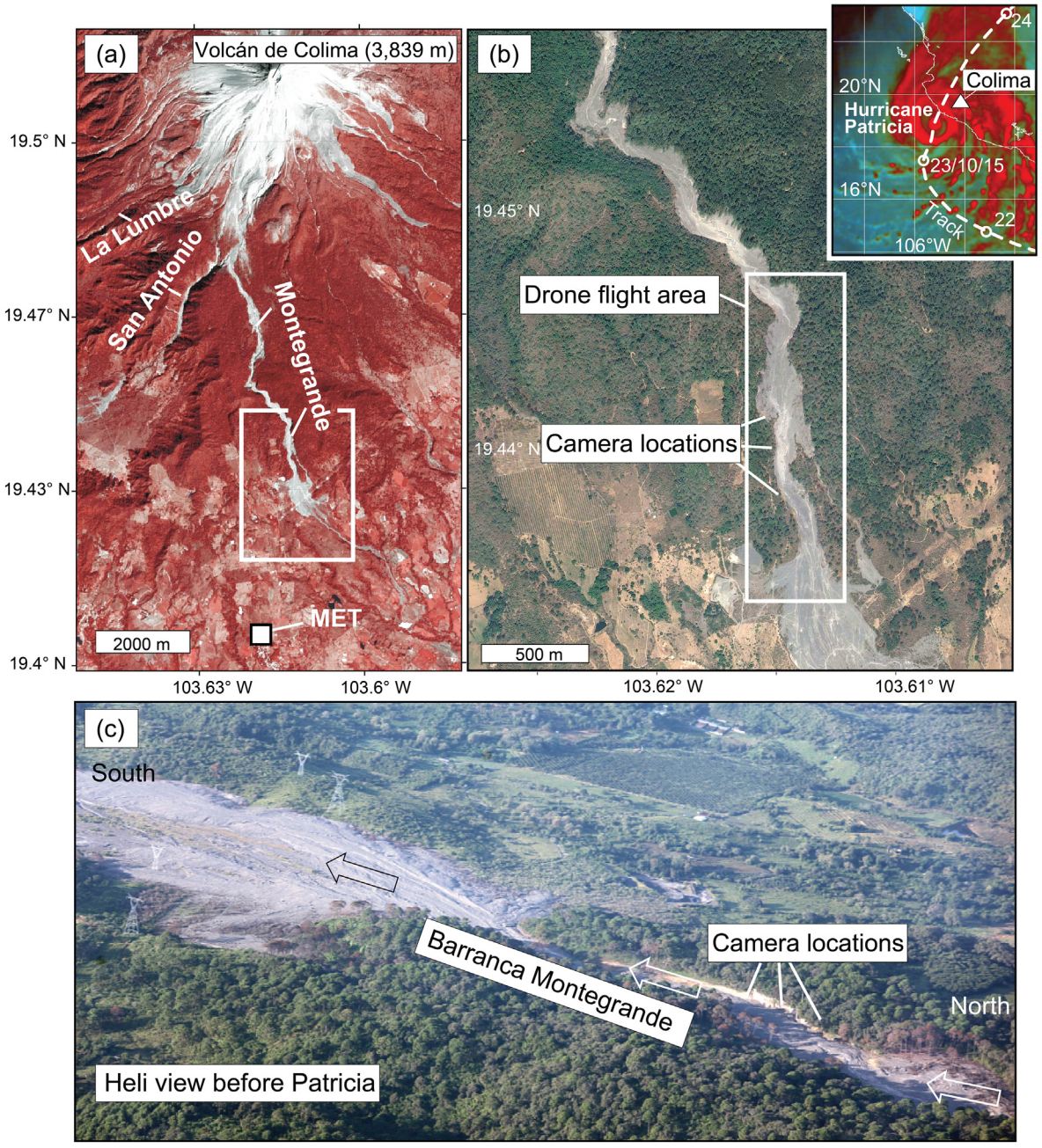

Fig. 1. Study area. (a) Satellite image of Volcán de Colima (Landsat 8, composite bands 5-4-3, pansharpened, 20160110); the Montegrande ravine is heading southwards and was channelling material transport from the volcano in 2015. MET is the location of the meteorological station and the seismic station shown in Fig. 2. (b) Montegrande ravine pyroclastic density currents (PDC) from July 2015. White box illustrates area studied by camera drones. Time lapse trail cameras are illustrated. Inset shows satellite image (91-GHz GPM) at 20:23 UTC on 23 October with location of Hurricane Patricia location just prior to landfall at the southwestern coast of Mexico. Courtesy Naval Research Lab, modified after (Kimberlain et al., 2016). White dashed line and circles: Track positions for Hurricane Patricia, 22–24 October 2015. Triangle: location of Volcán de Colima. (c) The Montegrande valley developed major lahars. Volcano is to the right (north).

2.2. Time-lapse cameras

Time-lapse camera images allow the visualization of changes at volcanoes from different perspectives and with a high spatial and temporal resolution. At Volcán de Colima their value as an efficient monitoring tool complementing other data has been previously demonstrated (Walter et al., 2013). Low cost weatherproof time lapse cameras were set up 48 h prior to the occurrence of the lahars in the Montegrande ravine. We strapped trail cameras (type Bushnell Trophy) to stable trees about 10 m above the ravine (Fig. 3h) at three different locations (Fig. 1b). The cameras were time synchronized and used in time-lapse mode, and were set to record an image at 5 million pixel resolution every 10 min, allowing the identification of changes in space and time. Shaking of the trees during the high hurricane winds was corrected using the digital image correlation (DIC) approach (Walter, 2011). Correlation plots were created for all images, here shown for images before and after the hurricane; using a search mask of 3 pixels. Results helped the verification of lahar occurrence and erosion details. Pixel to metre scaling was performed by measuring the location of prominent features in the field of view by GPS and by considering georeferenced photomosaic datasets from the UAV close range photogrammetry campaigns as detailed below.

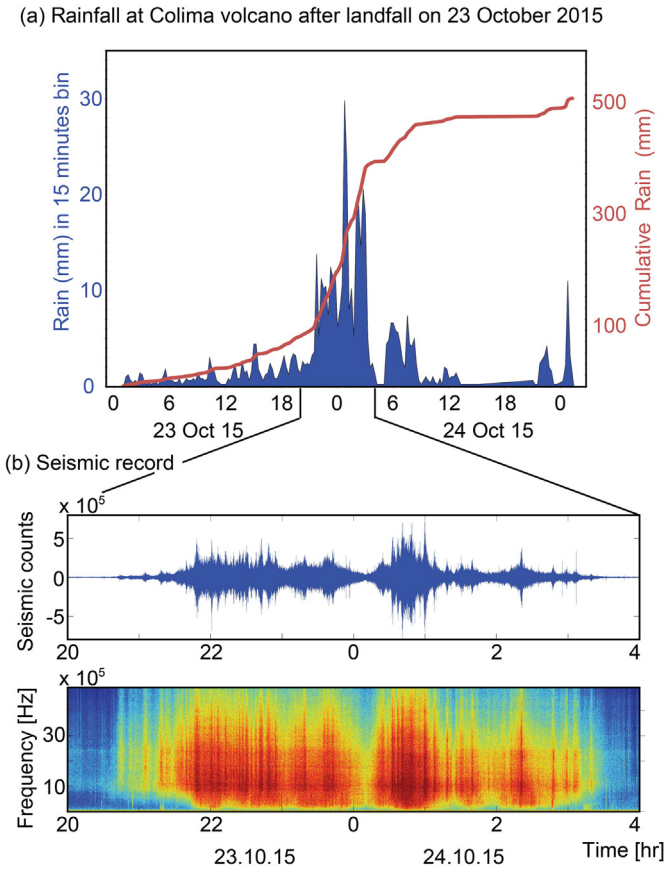

Fig. 2. (a) Rain data from Montitlán (see MET in Fig. 1a), showing accumulation of 500 mm within 48 h. Higher rainfall is expected to have occurred at higher elevations. Rainfall occurred in two main pulses. (b) Seismogram of the lahar and its corresponding spectrogram recorded by Montegrande seismic station. Lahar started at 20:40 on 23-Oct-15 and finished at 02:25 on 24-Oct-15 (UTC). The occurrence of the lahar thus well correlates with the amount of rainfall. Frequencies mainly fall between 10 and 40 Hz, dominant near 10 Hz.

2.3. UAV close range photogrammetry

Unmanned aerial vehicles (UAVs) are increasingly used in geosciences, thanks to their efficiency and flexibility for observing geological processes and acquiring data from different attached instruments, e.g. (Amici et al., 2013; Mancini et al., 2013; Nakano et al., 2014; Müller et al., 2017). Various platforms and techniques are available, ranging from multicopters to kites and balloons (Carrivick et al., 2013; Al-Halbouni et al., 2017), allowing especially wide application in the field of photogrammetry and remote sensing (Colomina and Molina, 2014). Close range aerial photogrammetry, processed by modern computer vision approaches, allows the derivation of a digital elevation model at very high resolution (James and Varley, 2012). We used a camera quadrocopter drone (DJI Phantom 3 pro) that was GPS controlled, and set up with a 12 million pixel resolution camera recording 30 geotagged images per flight minute, stabilized by a 2-axis gimbal to absorb vibration artifacts in the images that are common for multirotor copters (Fig. 3h). In addition, we measured 20 Ground Control Points (GCPs) by GPS distributed over the study area. The flight path was pre-configured by flight controlling software (Map Pilot App), and the same path was flown before and after the hurricane. In total 1200 high quality images were recorded, which were then processed using the Structure from Motion and Multi-View Stereo (SfM-MVS) approach included in the Photoscan Pro software package (version 1.3.5), similar to the approach used in other studies (Johnson et al., 2014). After quality checking and aligning the photos, we calculated the dense point cloud composed of ~24–30,000,000 points for each of the data volumes (before and after the hurricane) in two separate chunks.

The pre-hurricane dataset (chunk 1) contains 425 images, out of which 407 are well aligned, with an effective overlap higher than 80% between images. The raw point cloud consists of 222,000 points with an RMS reprojection error of 1.9 pixels, computed with medium alignment accuracy and generic preselection. After optimizing camera parameters, we reconstruct a dense point cloud, now achieving 24,364,000 points. The pre-hurricane surface reconstruction contains 1,623,000 faces and generation of an orthomosaic of 17,992 × 53,996 pixels and a resampled digital elevation model of 14.7 cm/pixels dimension in the WGS 84 coordinate system. Chunk 2, after the hurricane, contained 617 aligned photos, with an effective overlap of 84% between images. The raw point cloud consisted of 301,000 points, with an RMS reprojection error of 3.3 pixels. The higher error likely resulted from less sunlight during this second drone overflight. The dense point cloud consisted of 31,011,000 points and allowed a surface reconstruction containing 2,067,000 faces, generation of an orthomosaic of 22,252 × 47,180 pixels and a resampled digital elevation model of 17.7 cm/pixels dimension. More details are provided in Table 1. The resulting DEMs with resolutions between 0.177 and 0.147 m were resampled to 0.3 m. Further data handling was realized using GIS-analysis.

2.4. GIS-analysis

We post-processed and analysed the data in GeoInformaticsSystem (GIS) Software ArcMap (v. 10.2.1). For this we added the rasterized datasets of the digital elevation models and of the orthomosaics before and after the hurricane. By using the ArcToolbox suite we used the digital elevation models to generate hillshade grey images, sun azimuth 315° at 45° (cf. Fig. 6), which allowed qualitative comparison of the pre- and post-hurricane datasets. Using a pixel-over-pixel comparison we then compute the difference between the two digital elevation models (cf. Fig. 7c). Interpolated lines allowed the derivation of sections through the available data, such as through the DEM difference, but also along the topography (Fig. 7c).

Furthermore, to further analyse the morphology and identify subtle changes in the downslope direction we create aspect maps, created using the ArcMap Spatial Analyst python command outAspect in arcpy. Aspect maps basically show the slope direction, where one computes the plane to the z-values of a moving window of dimensions 3 × 3 cells, cell values indicating the compass direction (in azimuth clockwise), so that the change in x and y direction is calculated by:

$$\frac{\partial z}{\partial x} = \frac{1}{8}((c + 2f + i) - (a + 2d + g)) \quad (1)$$

and

$$\frac{\partial z}{\partial y} = \frac{1}{8}((g + 2h + i) - (a + 2b + c)), \quad (2)$$

Table 1
Comparison of data and processing parameters for the two datasets.

	Chunk 1 (before Patricia)	Chunk 2 (after Patricia)
Images selected	425	650
Aligned images	407	617
Markers used	20	20
Coordinate system	WGS 84 (EPSG::4326)	WGS 84 (EPSG::4326)
Point cloud	190,696	300,925
RMS reprojection error	1.93587	3.31089
Effective overlap	81%	83%
Dense point cloud	24,346,368	31,011,173
Surface faces	1,623,090	2,067,403
DEM	4498 × 13,499	8489 × 16,755
Resolution	14.7 cm/pix	17.7 cm/pix
Orthomosaic	17,992 × 53,996	22,252 × 47,180

where the changes (∂) are indicated at the cells identified as letters *a* to *i*, with a 3 × 3 arrangement, upper left being the *a* and lower right being the *i*, and *e* being the centre cell (Burrough and McDonell, 1998), so that the aspect value

$$\text{aspect} = 57.29578 * \text{atan2}\left(\left[\frac{\partial z}{\partial y}\right], -\left[\frac{\partial z}{\partial x}\right]\right) \quad (3)$$

is then converted to azimuth compass direction values (0–360°). These aspect maps help the identification of those rills and gullies that strike differently than the main central erosion gully, clarifying the different morphometry of erosion forms.

We use the digital elevation maps further for slope map analysis. Similarly as in the above described aspect map function, we fit a plane to the z-values of a moving window with dimensions 3 × 3 cells. We use an atan-function to solve the differences of the surface in the horizontal and vertical directions from the centre cell, so that lower slope values are depicting a flatter terrain. These slope calculations are used for identifying the steep nature of the central erosion channel (cf. Fig. 8).

3. Results

3.1. Lahar signals

Hurricane Patricia made landfall on 23 October 2015. Rainfall data measured near to the Montegrande ravine shows rapid intensification starting around 15:00 local time (20:00 UTC). The cumulative rainfall during the passage of the hurricane recorded at this location was about 500 mm (Fig. 2a). Maximum intensity rainfall lasted about 5 h, and was followed by a weaker episode of rain later that night, starting at 20:45 local time and lasting ~80 min. The meteorological measurements confirmed the rain band structure that had been suggested based on satellite imagery (Kimberlain et al., 2016).

The start of the lahar was recorded at the seismic station at about 15:40 local time (20:40 UTC) on 23 October, and it terminated at 22:25 (03:25 UTC), giving a duration of 6 h and 45 min approximately. The seismic record showed the clear occurrence of the lahar, with a characteristic high frequency component ranging from below 10 up to 40 Hz (Fig. 2b), and with seismic amplitudes that allowed the identification of the main flow pulses. The lahar started relatively weak, had a long duration and slightly decreased in amplitude and frequency (from >40 Hz to ~20 Hz), before another very pronounced but short pulse was recorded (Fig. 2b), followed by smaller pulses and a long-duration coda. A direct relationship between the rainfall intensity and the seismic signature of lahar occurrence appears evident. The characteristics of these seismic records are well identified at this seismic station and interpreted to be related to the Montegrande ravine, where we could measure the erosional effects of the lahar in detail.

3.2. Field inspection

Field inspection two days after the lahar event revealed a number of new pronounced erosion features and significant geomorphologic changes, as illustrated in Fig. 3. The sediments subject to erosion in the Montegrande ravine are highly unconsolidated deposits from pyroclastic density currents (PDCs) from the 7/2015 eruption. We found geomorphological features that are common in soft sediments on hillslopes: In the middle of the Montegrande ravine, we observed steep central channels, eroded with near-vertical cliffs that lead to bank erosion and slumps of the PDC deposits into the central channel (Fig. 3a). Wider networks of erosion gullies were developed, the erosion accumulating to several metres (Fig. 3b). Erosion at the margins of the Montegrande ravines led to undercarving of the older deposits and rockfalls, some exceeding a 7 m free fall (Fig. 3c). These commonly emerged at places where smaller streamlets merge and flow into the main ravine. At some places the deep central gully erosion branched into deep rill channels (Fig. 3d), that form networks and feed the major channels (Fig. 3e). Gradual progression of the rill channels is evident, from sub-centimetre scale to decimetre scale. Where the original PDC surface remained, evidence for rain splash erosion and overland flow were widespread, developing into rills, leading to small riplets with fine grained sedimentation in their troughs (Fig. 3f). This surface texture is characteristic for heavy rainfall regions. At the lithology contact between the PDC and the ravine bedrock, we observe deep gullies (figure g). These deep gullies can often be traced over hundreds of metres along the Montegrande ravine margins, occasionally evident at either side of the ravine. Small rills or gullies develop from these marginal erosion features into the centre of the ravine.

3.3. Time lapse camera results

Fixed installed cameras reveal that both localized deep (rill and channel) erosion as well as widespread inter-rill erosion (overland flow) occurred. This is shown for three installed trail cameras (Fig. 3h) located on the western flank of the Montegrande ravine, with a field of view to the north, northeast and east (cam a–c in Fig. 4). Images taken before Hurricane Patricia show the 2015 pyroclastic deposits as a terrain without vegetation, with isolated large and sub-rounded boulders (the largest boulder shown in Fig. 4a, left side, measures 1.3 m across), and localized erosion with vertical cliffs at the floodplains not exceeding a few tens of centimetres. Image quality during the occurrence of the lahar was poor, and mainly hindered by the reduced sunlight, water droplets on the lens and pronounced steaming. The fact that localized fog or steaming was observed along the ravines, indicates a heated lahar and/or hot PDC deposit now excavated by erosion (Fig. 4a centre image). After the lahar, major relief changes were observed: camera “a” showed small ripple formation (Fig. 4a). Camera “b” showed deposition of material in the centre of the ravine, while erosion of the sides increased, gradually forming terraces (Fig. 4b). Camera “c” showed the erosional gully formation located at the valley walls, i.e. at the lithology contrast between the flood plain and the ravine bedrock (Fig. 4c). Especially the areas located closer to the three cameras' field of view appear with a higher contrast after the hurricane than before. Closer inspection shows that this is due to abundant small scale rivulets that drained the overland flow of sediment-laden water.

As seen by the camera data, even though some sections of the Montegrande valley ravine did not display any deep erosion gullies, evidence for overland flow and small scaled erosion processes are extensive. In fact, as loose small-grained material has been mobilized, we find a deepening of the numerous little streamlets, rills and eroded channels in close-up views (Fig. 5). While the location of the abundant small erosion rills appears predefined by small irregularities already present before the hurricane, we find a deepening thereof to a depth commonly exceeding 5 cm, reaching up to 10 cm at selected outcrops, with very constant spacing on the order of 0.35 m in selected sections (Fig. 5c) allowing inferring erosion volumes for this particular location as discussed below. This pronounced change in image features is well monitored by correlation plots, where images before and after the hurricane show a generally lower agreement. The correlation of two images taken at similar times of day before the Hurricane has a generally higher pixel-wise intensity correlation than images compared before and after the event. These are represented by point clouds in the correlation diagrams that show systematically stronger scatter after the hurricane, likely associated with different forms of erosion ranging from rain splash to gully erosion (Fig. 4, right column). The information we are drawing from these simple time-lapse photo records is that erosion is multiscale, on one side concentrated in deep channels, and on the other hand being widespread over the entire region investigated. A more quantitative assessment on these multiscale erosion features is realized by drone data, as described in the following section.

Fig. 3. (a) Field photographs illustrating different types of erosion in the Montegrande valley (a–g) and the camera devices used for monitoring geomorphological changes (h). See text for more details.

Fig. 4. Fixed installed trail cameras allowed the time lapse monitoring of changes in the Montegrande ravine from three perspective views (a–c, view to the east, northeast, north, camera location is shown in Figs. 1 and 2). Images from the lahar itself (middle figure column) are of poor quality, but clearly show their occurrence. Deep erosion occurs locally, but also rill erosion is widespread. The terrain appears rougher after the hurricane due to removal of loose ash from the surface. A close-up of the white box in (a) is provided in Fig. 5.

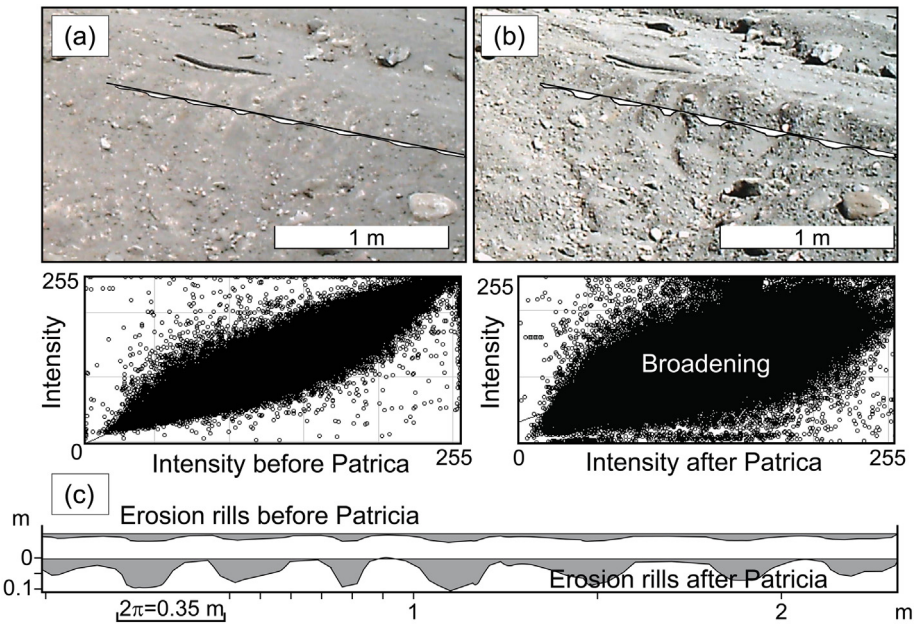

Fig. 5. Close-up showing example of small scale rill erosion and development of erosion rills. The correlation plots provide a means of identifying the degree of changes between images, where correlation between 2 images before the hurricane is high, whereas correlation between an image before and an image after the hurricane is constantly low. (c) Erosion along profile given in a–b with depth from 1–2 cm before to 6–9 cm deep rills after the rain event. (c) The rills appear very regular at 35 cm distance.

3.4. Drone photogrammetry results

Total UAV flight distance was 22 km (realized with multiple battery recharges) and hence a 2 km long stretch covering ~200,000 m^2 of the Montegrande ravine could be mapped in detail before and after the hurricane. The location of the surveyed area and analysis results are provided in Fig. 6, showing the digital terrain models before and after the hurricane, respectively. The locations of ground control points used for creating referencing both terrain models are distributed over the study area, as illustrated in Fig. 6a. We find that the two datasets are very well co-located, with a systematic location error better than 0.08 m.

Digital elevation model comparison reveals the localized and intense erosion in the region (Fig. 7). Erosional gullies are steeply incising and follow the slope, the path of pre-existing erosional gullies, and the margins of the pyroclastic infill of the Montegrande ravine. From the digital elevation data before and after we compute a height difference map, revealing regions of erosion and deposition. We can identify an alternating erosion-deposition pattern, which is somewhat systematic with a 320 m wavelength (Fig. 7d). Deposition appears to occur at those zones of decreasing slope (Fig. 7c), while local highs are eroded to form small traverse valleys, such as at the location of the deepest erosion (Fig. 7c, d).

Morphology close-up view before the hurricane showed pronounced but thin erosion rills that propagate into locally steep central channels (Fig. 8a). The deepest parts of the central erosion channel is commonly confined to a width <5 m, having near vertical walls, meandering downslope (Fig. 8c). The morphology next to this erosion channel is relatively smooth, with widespread unconsolidated sands and silts and a few isolated boulders. Close-up view after the hurricane reveals profound deepening and widening of the aforementioned rills and central erosion channel (Fig. 8d), now generally >10 m wide, with near vertical flanks and a flat plain in its centre (Fig. 8f, i). Channels that eroded during the hurricane in the middle of the Montegrande ravine are repeatedly widening and narrowing. The length of the deep central channel (Fig. 8) is 120 m, then it almost disappears for about 150 m (Fig. 8h) before showing again as a several metre deep eroded channel. Difference calculations of the two DEMs (Fig. 8h) reveal a localized erosion depth exceeding 4 m in the central channel (profile insert in Fig. 8i). In terms of maximum volumetric differences, we observe a material loss (erosion) of 15.5 m^3 per investigated metre along the ravine, and a deposition of 6 m^3 per metre along the ravine. Mean values of erosion and deposition over the 2 km long study area are 5.5 and 0.6 m^3 per metre along the ravine, respectively.

Although deepening of existing gullies dominates, a closer inspection of the data reveals that the erosion is often localized along the margins of the pyroclastic deposits (Fig. 8d, f). These deep erosional zones are identified at the marginal contact interface of pyroclastic infill, being the lithological boundary between the river bed/streamflow sands and the vegetation on the lateral soil and bedrock. Interestingly, the comparison of the aspect maps before and after the hurricane, clearly depicts the longitudinal central channel, having larger width and minor meandering only after the lahar (Fig. 8b, e). In addition we can make the widespread observation that in the formerly flat region of the PDC deposits, now a higher roughness emerges, which may indicate overland flow and rain splash erosion rills similar to those observed in the time-lapse cameras.

Evidences for overland flow and formation of rill erosion are further examined in Fig. 9, which is in a low slope area where we expected sedimentation instead of erosion and bulking processes. Aspect maps identify an erosion gully before and after the lahar, in a location flanking a central channel (left side of Fig. 9a, b). While small scale channel levees oriented along the flow direction partially disappear after the lahar, we observe that the topographic rills in the periphery of the central channel become stronger expressed, here with a direction towards the central channel. Difference of the two digital elevation models along a profile normal to these rill erosion features highlights a topographic change of up to 0.2 m and development of rills at 4–5 m intervals (Fig. 9c), hence at a larger scale than the identified 0.35 m further upstream (cf. Fig. 5). Therefore, erosion and accordingly bulking occurs also at this zone investigated, though the scale of overland flow and erosion strongly varies.

4. Discussion

Tephra-covered hillslopes are eroded by inter-rill and rill erosion processes (Bryan, 2000), both of which could be well identified at Volcán de Colima following a 22–23 October 2015 hurricane. Our study of the

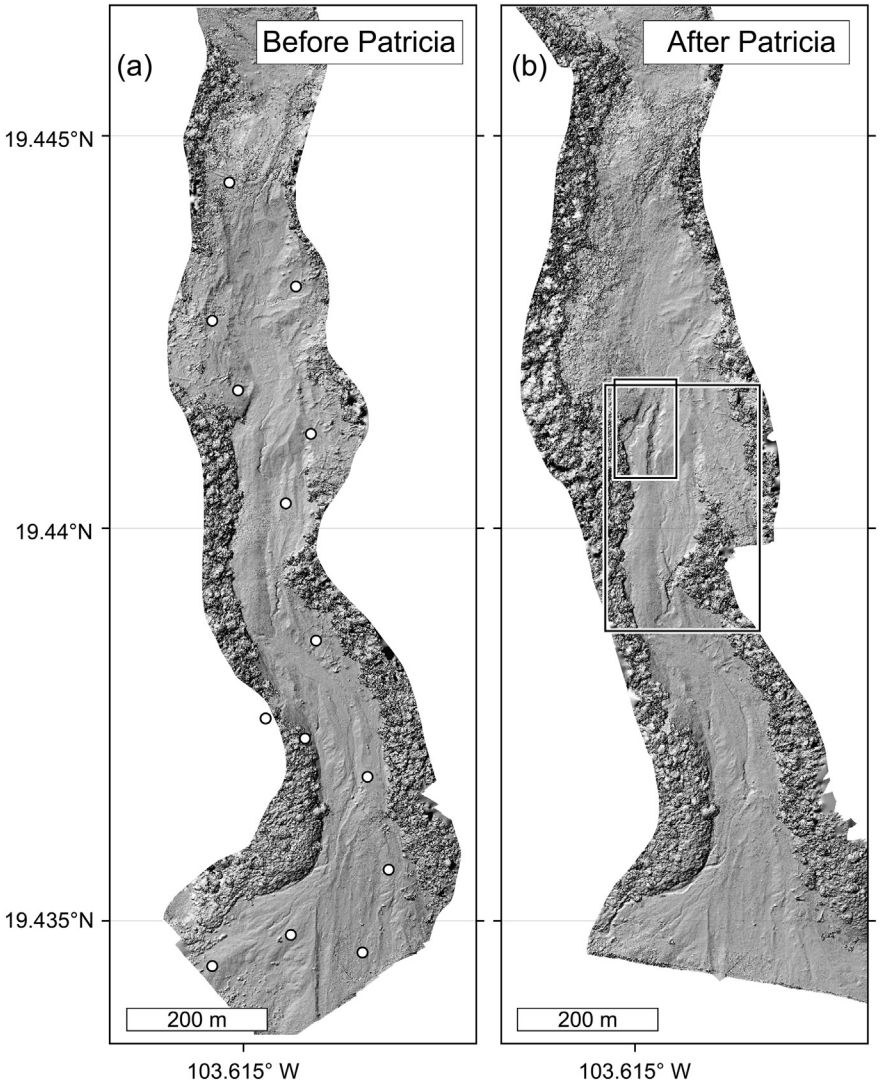

Fig. 6. Shaded relief maps derived from camera drone data acquired (a) 2 days before the hurricane and (b) 2 days after Hurricane Patricia. Drone data allowed mapping morphological changes associated with the 23 October 2015 lahar. White circle symbols in (a) represent ground control points as measured by GPS. Inset boxes show locations of close ups in Fig. 8.

geomorphologic changes allowed determining the complexity of erosion, alternation with deposition and the different scales of erosion ranging from overland flow and small rills to major central erosion channels exceeding 4 m in depth.

4.1. Topographic mapping developments

Understanding of lahar hazards, in specific, has been greatly advanced by modern monitoring systems, including LiDAR, seismology, infrasound, and fixed installed IP-cameras (Lavigne et al., 2000; Vázquez et al., 2014; Wibowo et al., 2015), allowing the study of the lahar dynamics, but also the quantification of the morphologic changes associated with lahars, erosion and deposition. Morphologic data acquisition shortly before and after an individual lahar occurrence nevertheless remains challenging, due to the unpredictable nature of the phenomenon. LiDAR airborne measurements, for instance, are ideal in terms of quality and resolution, but commonly too costly to be realized at close time intervals. Ground based LiDAR, or terrestrial laser scanning (TLS), might in turn allow highest resolutions of topographic point clouds to be acquired that are available for assessing volcano morphologies and structures (Richter et al., 2016), but require landscapes that allow a number of good viewpoints onto the surface to be studied. Therefore, strategies are proposed to combine TLS and photogrammetric data, as realized at Merapi volcano (Darmawan et al., 2018) or on Holuhraun volcano (Müller et al., 2017). However, as TLS is costly, its application in volcanology has remained relatively rare, especially for generation of repeat survey data. And it has to be noted that studies comparing topographic data before and after events may miss the processes occurring during the event, as suggested in Gomez et al., 2018.

Cost-effective data for the end-user is often realized by satellite remote sensing, where digital elevation models are derived at steep sided volcanoes from optical (Salzer et al., 2017) or radar satellites (Kubanek et al., 2015) and may even provide the temporal and spatial resolution to identify changes within weeks to months (Walter et al., 2015). Disadvantage is that these techniques commonly require close and well planned data acquisition strategies in advance that are difficult to realize for many regions, the data often remained restricted to few users, and the spatial resolution of optical and radar data is generally 1–5 m and 10–15 m at its best, respectively. Therefore, small scaled geomorphologic changes associated with lahars require different techniques to be employed. In this article we found camera drones to be well suited for investigating the morphological changes on the flanks of Volcán de Colima, with a very high resolution (0.01–0.2 m resolutions) and flexible use (daily revisits possible). The advantage of camera drones if compared to aforementioned methods has been recognized already elsewhere (Nakano et al., 2014; Müller et al., 2017; Darmawan

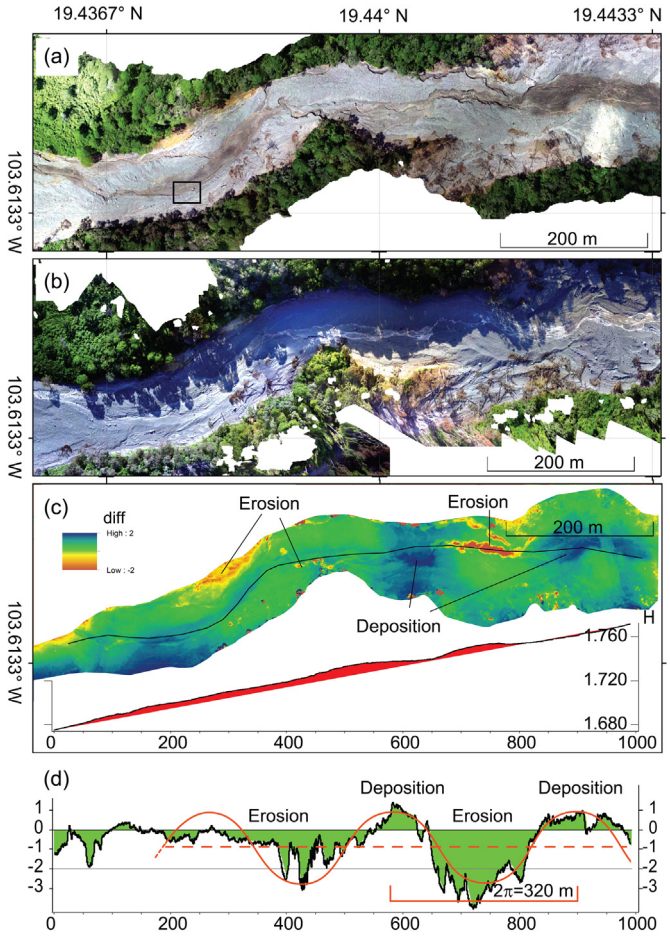

Fig. 7. Air photo mosaic before (b) and after (a) the lahar. Difference between digital elevation models reveals sites of erosion alternating with deposition (c). Erosion maxima locally concurs at area of slope changes and valley margin. (d) Profile along centre of valley (20 m width average) illustrates alternating erosion and deposition, at recurrence of 320 m in this section.

et al., 2018), providing coherent and shadow free data for geomorphologic studies at steep sided volcanoes.

As soon as the United States National Hurricane Centre forecasted the timing and location of Hurricane Patricia, in a rapid response action we acquired drone-based close range aerial photography data in the Montegrande ravine, underlining the highly flexible use of these instruments. Two days after the hurricane had landfall, we could reoccupy the site again and use the drones a second time. Therefore, the new developments in drone-based topographic mapping allowed us to identify lahar-related erosion and deposition effects in close detail, distinguishing large scale erosion gullies, small scale erosion rills, overland flow, terrain slope and aspect changes. Before further discussing the implications of this work, we discuss a number of limitations.

4.2. Limitations

Drone based photogrammetric datasets have many advantages, but are subject to a number of limitations that are important to understand. Instrumental noise may come from the camera used. As our drone is equipped with a camera with a 1/2.3″ CMOS sensor and a gimbal to reduce vibration artifacts, in good light conditions we obtained very high image qualities. We recognized, however, that in those images of strong brightness contrasts (due to half shadow), local camera exposure compensations occasionally remained challenging. Our flights were realized at different cloud cover, which results in different illumination and shadowing effects. While this is not ideal for photomosaic comparison these visual brightness changes have no significant relevance for the quality of the digital elevation model and our geomorphologic analysis, as the comparison in resolution and errors reveals (see Table 1).

We set the drone camera to time-lapse mode, at 30 frames per minute. This time-lapse mode is used rather than a higher frame rate video mode, as the video acquisition mode of our drone performs an image stabilization, which might result in unwanted wobbling and distortion effects. Furthermore, we experienced environmental limitations mainly related to moisture and rain. During the hurricane, visibility was near zero, we therefore can only analyse the topographic changes that occurred before and after the hurricane, and interpret them to be related to the hurricane rainfall-induced lahar.

Using this available dataset we are not able to identify isolated lahar pulses associated with banded rainfall, as hypothesized from the pulsating behaviour in the seismograms, likely related to the occurrence of several lahar pulses. The hurricane locally produced about half a metre of rainfall within only 6 h, which is approx. half of the total annual precipitation (800–1000 mm), if compared to data from the National Water Commission (Comisión Nacional del Agua, CNA, http://smn.cna.gob.mx/). Notably, at locations higher on the mountain, rainfall may have started earlier and was likely more intense. Significant rainfall damage continued at Volcán de Colima, as another late 2015 tropical storm followed Patricia. Here we have no field evidence for deep erosion, however.

This study concentrates on effects in the Montegrande ravine. However, we note that this was not the only ravine subject to the occurrence of a lahar on 23 October 2015 (Vázquez et al., 2016). In fact, scientists and Civil Protection expected lahars in a number of different ravines, the strongest two of them being in the Montegrande ravine and in the La Lumbre ravine, the latter being further to the West (Vázquez et al., 2016). The La Lumbre lahar was highly destructive and damaged buildings, roads and bridges, and was further investigated in an independent study (Capra et al., 2018a). As we could not cover all possible lahar sites by drone flights prior to the hurricane, we herein focus on the Montegrande ravine.

We utilized GPS based ground control points that contributed to the alignment and georeferencing of the two point clouds (see also Table 1). As the Montegrande ravine was completely composed of unconsolidated pyroclastic material from the 2015 eruption and previous deposits, we could not measure solid basement locations by GPS, but had to rely instead on the stability of large boulders. These might have been moved or rotated during the hurricane. Given the small errors (<3 pixels) we determined during the SfM-MVS processing, however, we assume that this effect is negligible.

4.3. Implications

The 2015 Volcán de Colima eruption created a summit crater open to the south (Reyes-Dávila et al., 2016) and deposition of unconsolidated material on steep terrain and in narrow ravines (Capra et al., 2016; Vázquez et al., 2016). Given this topographic setting, the 2015 lahar events were in fact anticipated.

The central part of the Montegrande ravine displayed an alternating erosion-deposition pattern, similar as has been observed at volcanoes elsewhere (Procter et al., 2010). The erosion features located in the centre of the ravine, in specific, exceeded 4 m in depth, and displayed a scale of morphological change that could even be identified with satellite images (Capra et al., 2016).

We could identify sediment entrainment mechanisms relevant for the lahar bulking processes, such as inter-rill and rill erosion processes (See Fig. 10.). Inter-rill erosion is related to rain-splash, whereas rill erosion is related to a more channelized runoff (Bryan, 2000).

While the direct effect of rain-splash on the sediment budget of lahars is probably small, its effect for initiation erosion processes can be significant (Bryan, 2000). The kinetic energy of the raindrops is dependent on the impact velocity, and therefore by wind, which is why this effect during hurricane force winds might be much larger

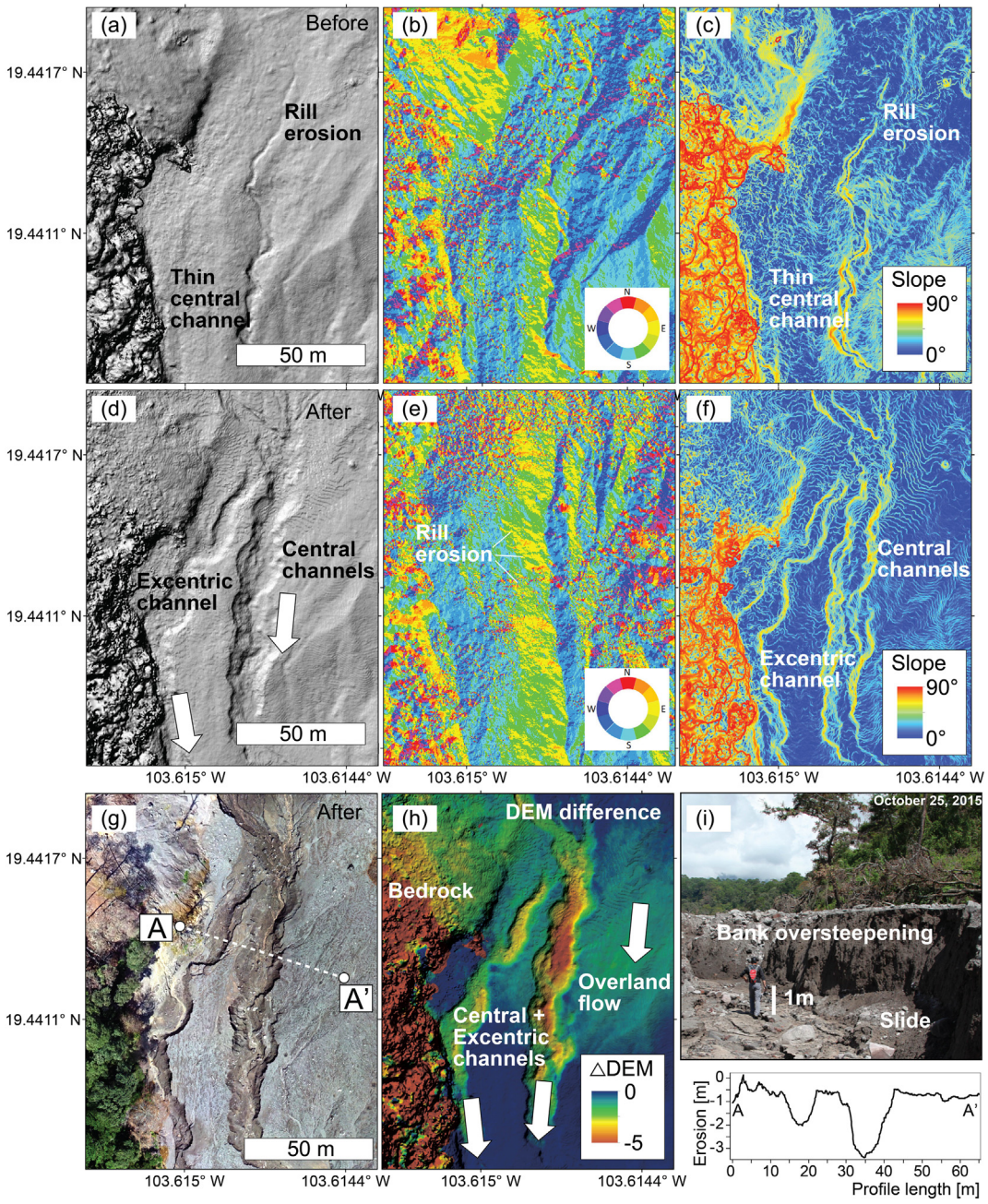

Fig. 8. Localized deep erosion directly related to the 23 October 2015 lahar. Top row is before (a, b, c), centre row is after the lahar (d, e, f). Comparison of before-after data reveals pronounced erosion along pre-existing small gullies (central channel) but also along the contact interfaces of the pyroclastic lithology to the valley margins (excentric channel). Aspect maps (b, e) reveal changes in the localized channels, but also widespread. Slope maps (c, f) reveal the steep sided erosion channels. Difference between the digital elevation data before-after (h) suggests encarving exceeding 4 m, which is confirmed by drone airphotos (g) and field inspection (i). Profile of topographic change (i subset) along A–A′, for location see (g).

than during rainfall only. The splash process is high on slopes where water drainage is persistent, whereas water ponding may decrease this effect. Channelization of the inter-rill erosion is seen by photogrammetric data in the Montegrande ravine, showing a darker and higher contrast material, associated with fine grained material, on small rill-like features. Inter-rill erosion depends on the initial erosion resistance of the soil, the slope, the runoff intensity and a surface roughness factor (Horton, 1945), however, these parameters are commonly difficult to measure in the field. We could identify such a fine grained erosion process, and therefore conjecture that unconsolidated tephra reduces the erosion resistance parameters, however, quantitative details of this process remain challenging to determine, and require higher resolution studies.

The inter-rill erosion, produced by overland flow, is largely unconfined, and may lead to localized small scale debris flows (Manville et al., 2000), underlining the significant contribution of this flow process to the bulking process of a lahar. On slopes, rain splash quickly develops into sediment-laden rill erosion, delivering the sediment and water to central channels. In this study we could add details on this rill erosion effect, quantify morphology changes and determine a regular rill spacing dependency. Rill erosion and channelization of sediment-laden waters are well identifiable due to the significant geomorphological and image intensity changes.

Fixed installed time-lapse cameras revealed the appearance of small erosion rills throughout the Montegrande ravine investigated. Although this data is providing merely a local snapshot, we use this information to

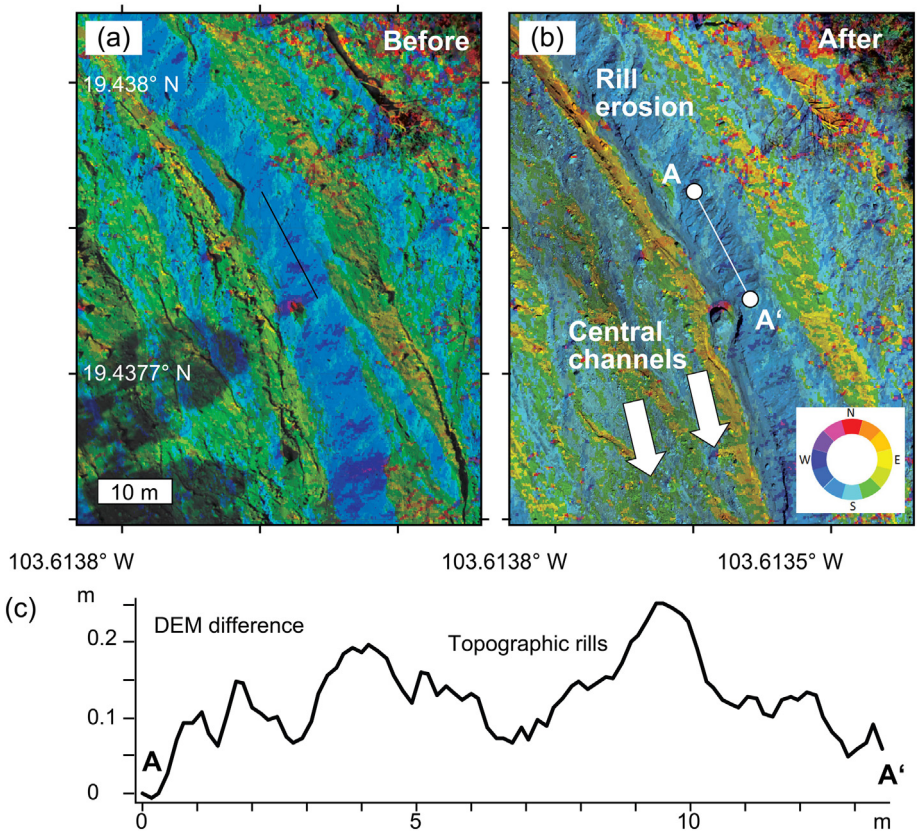

Fig. 9. Aspect maps before (a) and after (b) show channel erosion and associated pronounced and steep sided gullies, as well as small scale erosion rills and rougher terrain (c). Profile of rill erosion shows topographic change of up to ~0.2 m common at 1–5 m distance. Location is illustrated by black dashed box in Fig. 7a.

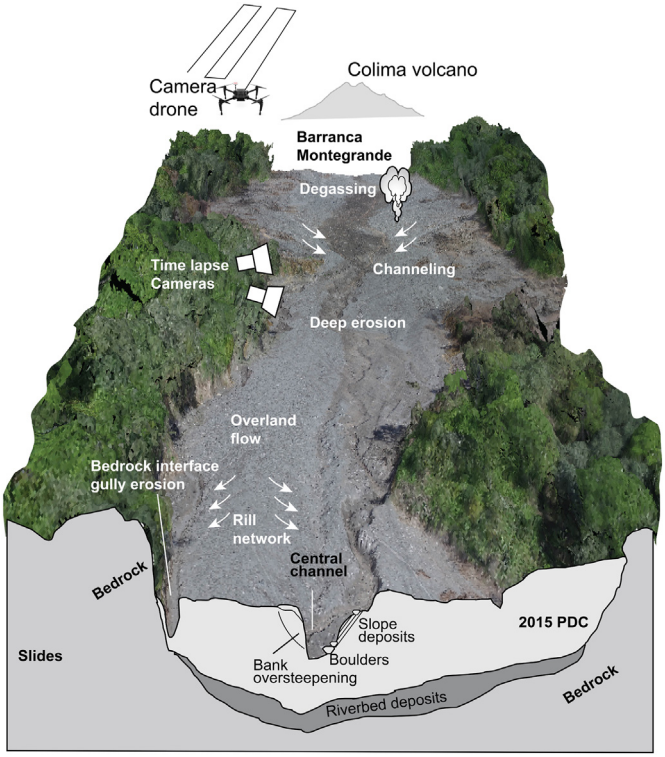

Fig. 10. Synthesis of different erosion forms and outcome of this study. Erosion forms identified are basal erosion, gully formation, undercutting and bank erosion, overland flow, rain splash and rill development, as well as lithology controlled erosion at bedrock interface near valley flanks.

speculate on the relevance of the widespread erosion. The spacing of the small erosion rills we identified is on average 5–15 cm, with a depth of generally 5–10 cm, often only 2 cm. Assuming an average erosion rill spacing of 10 cm, and conservative average rill depth of 5 cm with steep 45° flanks, then the material loss would accumulate to an average of 0.025 m^3 per m^2, possibly equally distributed over the 198,000 m^2 study area. Even though these numbers are highly site dependent and may largely vary along the ravine, we may highlight the significant role of inter-rill and rill erosion. In volume, this accumulates to 5000 m^3 over the study area. To compare, about 11,000 m^3 were removed in deep gullies (see Section 3.4), and 5000 m^3 removed by inter-rill and rill erosion. Therefore, the new and abundant small erosion rills contribute to an overland erosion volume that is approaching similar dimensions than the localized material loss in the main gullies that channelized the lahars. This material addition is considered as an important bulking process.

Similarities in the erosional nature exist between Volcán de Colima and Casitas volcano, Nicaragua, where Hurricane Mitch created intense rainfall in 1998 (Scott et al., 2005), causing a lahar that was steadily eroding and growing with distance indicative of a sustained bulking effect. We conjecture that similar situation occurred at Volcán de Colima in 2015, associated with a growing and eroding lahar at 8 km from the volcano. Similar observations were made at Casita volcano, where the growth of the volume downstream approached 2–3 times, due to addition of water-saturated sediments (Vallance, 2000).

Of additional interest also is the pronounced steaming observed in one section of the ravine. We observed steaming of the lahars deposits themselves, implying that some pulses at least were hot. At the study area, which is at ~8 km from the summit (Fig. 6), further information was gathered from our field visit directly after the hurricane passed. In the Montegrande ravine, the lahar eroded the recent 2015 pyroclastic

flow deposits, and there were signs of high temperature and bubbling groundwater streams, with water temperatures exceeding 80 °C. During the field visit we also observed regions of vigorous degassing and remnant wood fragments burnt by the 2015 PDCs. Curiously steaming and thermal anomalies seemed to have intensified in those regions of strong erosion. This could result from the erosion into a still hotter PDC deposit, and overburden unloading. Assuming a PDC density of 2300 kg/m^3 and an erosion depth up to 5.2 m, we calculate a unloading force of up to 120,000 N/m^2, which may guide hot groundwater towards the surface following pressure gradients (Schöpa et al., 2011). However, we could not identify a simple correlation between erosion depth and steaming intensity, which is why the nature of the steaming ground water as observed after the hurricane remains to be further explored.

5. Conclusion

Following the 07/2015 PDC producing eruption at Volcán de Colima, Mexico, a major hurricane with intense rainfall mobilized unconsolidated material, forming widespread lahar hazards and erosion of deep ravines on the volcano south flank. Realizing field campaigns just two days before and after the Hurricane, and obtaining drone-based and time lapse camera data, we (i) monitored morphologic changes associated with this particular lahar event, and (ii) retrieved spatial resolutions that allowed deciphering of even small scale geomorphologic changes. We identified different scales of overland flow (inter-rill) and rill erosion. We found abundant small erosion rills predefined by small irregularities already present before the hurricane. Erosion rills deepened and results also indicated a significant contribution of the inter-rill erosion contributing to the overall bulking and sediment redistribution during the hurricane. We further found the scales of overland flow and erosion strongly vary. Localized erosion exceeded four metres in depth in the central channel, which accumulated to a material loss (erosion) of over 15 m^3 per metre along the ravine. Maximum deposition, in turn, was 6 m^3. On average the erosion volume was about ten times the deposition volume. We describe longitudinal fluctuations of erosional gullies, and compare results to observations at other volcanoes, revealing that overall the hurricane-generated lahar exhibited characteristics similar to those observed elsewhere, but our approach allowed the close study of small scale erosion features at an unprecedented level of detail.

Acknowledgements

This is a contribution to VOLCAPSE, a research project funded by the European Research Council under the European Union's H2020 Programme/ERC consolidator grant No. [ERC-CoG 646858]. We appreciate discussion with Lucia Capra, and thank the two journal reviewers for very constructive comments that helped improve this article.

References

Al-Halbouni, D., Holohan, E.P., Saberi, L., Alrshdan, H., Sawarieh, A., Closson, D., Walter, T.R., Dahm, T., 2017. Sinkholes, subsidence and subrosion on the eastern shore of the Dead Sea as revealed by a close-range photogrammetric survey. Geomorphology 285, 305–324.

Amici, S., Turci, M., Giulietti, F., Giammanco, S., Buongiorno, M.F., La Spina, A., Spampinato, L., 2013. Volcanic environments monitoring by drones mud volcano case study. Uav-G2013, pp. 5–10.

Beverage, J., Culbertson, J., 1964. Hyperconcentrations of suspended sediment. Am. Soc. Civil Eng. 90, 117–126.

Bryan, R.B., 2000. Soil erodibility and processes of water erosion on hillslope. Geomorphology 32 (3–4), 385–415.

Burrough, P.A., McDonell, R.A., 1998. Principles of Geographical Information Systems. Oxford University Press, New York, pp. 1–190.

Capra, L., Macias, J.L., Cortes, A., Dávila, N., Saucedo, R., Osorio-Ocampo, S., Arce, J.L., Gavilanes-Ruiz, J.C., Corona-Chavez, P., Garcia-Sanchez, L., Sosa-Ceballos, G., Vazquez, R., 2016. Preliminary report on the July 10–11, 2015 eruption at Volcán de Colima: pyroclastic density currents with exceptional runouts and volume. J. Volcanol. Geotherm. Res. 310, 39–49.

Capra, L., Coviello, V., Borselli, L., Márquez-Ramirez, V.H., Arámbula-Mendoza, R., 2018a. Hydrological control of large hurricane-induced lahars: evidence from rainfall-runoff modeling, seismic and video monitoring. Nat. Hazards Earth Syst. Sci. 18 (3), 781–794.

Capra, L., Sulpizio, R., Márquez-Ramirez, V.H., Coviello, V., Doronzo, D.M., Arambula-Mendoza, R., Cruz, S., 2018b. The anatomy of a pyroclastic density current: the 10 July 2015 event at Volcán de Colima (Mexico). Bull. Volcanol. 80 (4).

Carrivick, J.L., Smith, M.W., Quincey, D.J., Carver, S.J., 2013. Developments in budget remote sensing for the geosciences. Geol. Today 29 (4), 138–143.

Colomina, I., Molina, P., 2014. Unmanned aerial systems for photogrammetry and remote sensing: a review. ISPRS J. Photogramm. Remote Sens. 92, 79–97.

Cronin, S.J., Neall, V.E., Lecointre, J.A., Palmer, A.S., 1997. Changes in Whangaehu river lahar characteristics during the 1995 eruption sequence, Ruapehu volcano, New Zealand. J. Volcanol. Geotherm. Res. 76 (1–2), 47–61.

Darmawan, H., Walter, T.R., Brotopuspito, K.S., Subandriyo, Nandaka, I.G.M.A., 2018. Morphological and structural changes at the Merapi lava dome monitored in 2012–15 using unmanned aerial vehicles (UAVs). J. Volcanol. Geotherm. Res. 349, 256–267.

Dávila, N., Capra, L., Gavilanes-Ruiz, J.C., Varley, N., Norini, G., Vazquez, A.G., 2007. Recent lahars at Volcán de Colima (Mexico): drainage variation and spectral classification. J. Volcanol. Geotherm. Res. 165 (3–5), 127–141.

Escudero, C.R., Bandy, W.L., 2017. Ambient seismic noise tomography of the Colima Volcano Complex. Bull. Volcanol. 79 (2).

Gomez, C., Lavigne, F., Hadmoko, D.S., Wassmer, P., 2018. Insights into lahar deposition processes in the Curah Lengkong (Semeru Volcano, Indonesia) using photogrammetry-based geospatial analysis, near-surface geophysics and CFD modelling. J. Volcanol. Geotherm. Res. 353, 102–113.

Horton, R.E., 1945. Erosional development of streams and their drainage basins: hydrophysical approach to quantitative morphology. Bull. Geol. Soc. Am. 56 (3), 275–370.

Hutchison, W., Varley, N., Pyle, D.M., Mather, T.A., Stevenson, J.A., 2013. Airborne thermal remote sensing of the Volcán de Colima (Mexico) lava dome from 2007 to 2010. Geol. Soc. 380, 203–228.

James, M.R., Robson, S., 2014. Mitigating systematic error in topographic models derived from UAV and ground-based image networks. Earth Surf. Process. Landf. 39 (10), 1413–1420.

James, M.R., Varley, N., 2012. Identification of structural controls in an active lava dome with high resolution DEMs: Volcán de Colima, Mexico. Geophys. Res. Lett. 39 (22), L22303.

Johnson, K., Nissen, E., Saripalli, S., Arrowsmith, J.R., McGarey, P., Scharer, K., Williams, P., Blisniuk, K., 2014. Rapid mapping of ultrafine fault zone topography with structure from motion. Geosphere 10 (5), 969–986.

Jones, J.W., Newhall, C., 1996. Preeruption and posteruption digital-terrain models of Mount Pinatubo. In: Newhall, C., Punongbayan, R.S. (Eds.), Fire and Mud: Eruptions and Lahars of Mount Pinatubo, Philippines. University of Washington Press, Philippine Institute of Volcanology and Seismology, Quezon City, Seattle and London, pp. 571–582.

Kimberlain, T.B., Blake, E.S., Cangialosi, J.P., 2016. Hurricane Patricia. National Hurricane Center Tropical Cyclone Report, EP202015(7), pp. 1–32.

Kubanek, J., Westerhaus, M., Schenk, A., Aisyah, N., Brotopuspito, K.S., Heck, B., 2015. Volumetric change quantification of the 2010 Merapi eruption using TanDEM-X InSAR. Remote Sens. Environ. 164, 16–25.

Lavigne, F., Thouret, J.C., Voight, B., Young, K., Lahusen, R., Marso, J., Suwa, H., Sumaryono, A., Sayudi, D.S., Dejean, M., 2000. Instrumental lahar monitoring at Merapi Volcano, Central Java, Indonesia. J. Volcanol. Geotherm. Res. 100 (1–4), 457–478.

Leung, M.F., Santos, J.R., Haimes, Y.Y., 2003. Risk modeling, assessment, and management of lahar flow threat. Risk Anal. 23 (6), 1323–1335.

Macías, J.L., Sosa-Ceballos, G., Arce, J.L., Gardner, J.E., Saucedo, R., Valdez-Moreno, G., 2017. Storage conditions and magma processes triggering the 1818 CE Plinian eruption of Volcan de Colima. J. Volcanol. Geotherm. Res. 340, 117–129.

Mancini, F., Dubbini, M., Gattelli, M., Stecchi, F., Fabbri, S., Gabbianelli, G., 2013. Using unmanned aerial vehicles (UAV) for high-resolution reconstruction of topography: the structure from motion approach on coastal environments. Remote Sens. 5 (12), 6880–6898.

Manville, V., White, J.D.L., Hodgson, K.A., 2000. Dynamic interactions between lahars and stream flow: a case study from Ruapehu Volcano, New Zealand: discussion. Geol. Soc. Am. Bull. 112 (7), 1149–1151.

Müller, D., Walter, T.R., Schöpa, A., Witt, T., Steinke, B., Gudmundsson, M.T., Dürig, T., 2017. High-resolution digital elevation modeling from TLS and UAV campaign reveals structural complexity at the 2014/2015 Holuhraun eruption site, Iceland. Front. Earth Sci. 5 (59).

Nakano, T., Kamiya, I., Tobita, M., Iwahashi, J., Nakajima, H., 2014. Landform monitoring in active volcano by Uav and Sfm-Mvs technique. Isprs Technical Commission VIII Symposium, 40–8, pp. 71–75.

Naranjo, J.L., Sigurdsson, H., Carey, S.N., Fritz, W., 1986. Eruption of the Nevado del Ruiz Volcano, Colombia, on 13 November 1985: tephra fall and lahars. Science 233 (4767), 961–963.

Pierson, T.C., Costa, J.E., 1987. A rheologic classification of subaerial sediment-water flows. Geol. Soc. Am. Rev. Eng. Geol. 7 (1-12).

Poli, D., Remondino, F., Angiuli, E., Agugiaro, G., 2015. Radiometric and geometric evaluation of GeoEye-1, WorldView-2 and Pleiades-1A stereo images for 3D information extraction. ISPRS J. Photogramm. Remote Sens. 100, 35–47.

Procter, J., Cronin, S.J., Fuller, I.C., Lube, G., Manville, V., 2010. Quantifying the geomorphic impacts of a lake-breakout lahar, Mount Ruapehu, New Zealand. Geology 38 (1), 67–70.

Reyes-Dávila, G.A., Arámbula-Mendoza, R., Espinasa-Pereña, R., Pankhurst, M.J., Navarro-Ochoa, C., Savov, I., Vargas-Bracamontes, D.M., Cortés-Cortés, A., Gutiérrez-Martínez, C., Valdés-González, C., Domínguez-Reyes, T., González-Amezcua, M., Martínez-Fierros, A., Ramírez-Vázquez, C.A., Cárdenas-González, L., Castañeda-Bastida, E., Espinoza de los Monteros, D.M.V., Nieto-Torres, A., Campion, R., Courtois, L., Lee,

P.D., 2016. Volcán de Colima dome collapse of July 2015 and associated pyroclastic density currents. J. Volcanol. Geotherm. Res. 320, 100–106.
Richter, N., Favalli, M., de Zeeuw-van Dalfsen, E., Fornaciai, A., Fernandes, R.M.D., Perez, N.M., Levy, J., Victoria, S.S., Walter, T.R., 2016. Lava flow hazard at Fogo Volcano, Cabo Verde, before and after the 2014–2015 eruption. Nat. Hazards Earth Syst. Sci. 16 (8), 1925–1951.
Salzer, J.T., Milillo, P., Varley, N., Perissin, D., Pantaleo, M., Walter, T.R., 2017. Evaluating links between deformation, topography and surface temperature at volcanic domes: results from a multi-sensor study at Volcán de Colima, Mexico. Earth Planet. Sci. Lett. 479, 354–365.
Schöpa, A., Pantaleo, M., Walter, T.R., 2011. Scale-dependent location of hydrothermal vents: stress field models and infrared field observations on the Fossa Cone, Vulcano Island, Italy. J. Volcanol. Geotherm. Res. 203 (3–4), 133–145.
Scott, K.M., Vallance, J.W., Kerle, N., Macías, J.L., Strauch, W., Devoli, G., 2005. Catastrophic precipitation-triggered lahar at Casita Volcano, Nicaragua: occurrence, bulking and transformation. Earth Surf. Process. Landf. 30 (1), 59–79.
Shen, H.O., Zheng, F.L., Wen, L.L., Lu, J., Jiang, Y.L., 2015. An experimental study of rill erosion and morphology. Geomorphology 231, 193–201.
Solikhin, A., Pine, V., Vandemeulebrouck, J., Thouret, J.C., Hendrasto, M., 2015. Mapping the 2010 Merapi pyroclastic deposits using dual-polarization Synthetic Aperture Radar (SAR) data. Remote Sens. Environ. 158, 180–192.
Spica, Z., Perton, M., Legrand, D., 2017. Anatomy of the Colima Volcano magmatic system, Mexico. Earth Planet. Sci. Lett. 459, 1–13.
Vallance, J.W., 2000. Lahars. In: Sigurdsson, H. (Ed.), Encyclopedia of Volcanoes. Academic Press, San Diego, pp. 601–616.
Vallance, J.W., Iverson, R.M., 2015. Lahars and their deposits. In: Sigurdsson, H., Houghton, B., McNutt, S., Rymer, H., Stix, J. (Eds.), Encyclopedia of Volcanoes. Academic Press, San Diego, pp. 649–664.
Vázquez, R., Capra, L., Caballero, L., Arambula-Mendoza, R., Reyes-Davila, G., 2014. The anatomy of a lahar: deciphering the 15th September 2012 lahar at Volcán de Colima, Mexico. J. Volcanol. Geotherm. Res. 272, 126–136.
Vázquez, R., Capra, L., Coviello, V., 2016. Factors controlling erosion/deposition phenomena related to lahars at Volcán de Colima, Mexico. Nat. Hazards Earth Syst. Sci. 16 (8), 1881–1895.
Walter, T.R., 2011. Low cost volcano deformation monitoring: optical strain measurement and application to Mount St. Helens data. Geophys. J. Int. 186 (2), 699–705.
Walter, T.R., Wang, R., Luehr, B.G., Wassermann, J., Behr, Y., Parolai, S., Anggraini, A., Gunther, E., Sobiesiak, M., Grosser, H., Wetzel, H.U., Milkereit, C., Brotopuspito, P.J.K.S., Harjadi, P., Zschau, J., 2008. The 26 May 2006 magnitude 6.4 Yogyakarta earthquake south of Mt. Merapi Volcano: did lahar deposits amplify ground shaking and thus lead to the disaster? Geochem. Geophys. Geosyst. 9 (Q05006), 1–9.
Walter, T.R., Ratdomopurbo, A., Subandriyo, Aisyah N., Brotopuspito, K.S., Salzer, J., Luhr, B., 2013. Dome growth and coulee spreading controlled by surface morphology, as determined by pixel offsets in photographs of the 2006 Merapi eruption. J. Volcanol. Geotherm. Res. 261, 121–129.
Walter, T.R., Subandriyo, J., Kirbani, S., Bathke, H., Suryanto, W., Aisyah, N., Darmawan, H., Jousset, P., Luehr, B.G., Dahm, T., 2015. Volcano-tectonic control of Merapi's lava dome splitting: the November 2013 fracture observed from high resolution TerraSAR-X data. Tectonophysics 639, 23–33.
Westoby, M.J., Brasington, J., Glasser, N.F., Hambrey, M.J., Reynolds, J.M., 2012. 'Structure-from-motion' photogrammetry: a low-cost, effective tool for geoscience applications. Geomorphology 179, 300–314.
Wibowo, S.B., Lavigne, F., Mourot, P., Metaxian, J.P., Zeghdoudi, M., Virmoux, C., Sukatja, C.B., Hadmoko, D.S., Mutaqin, B.W., 2015. Coupling between video and seismic data analysis for the study of lahar dynamics at Merapi Volcano, Indonesia. Geomorphology 21 (3), 251–265.
Zobin, V.M., Plascencia, I., Reyes, G., Navarro, C., 2009. The characteristics of seismic signals produced by lahars and pyroclastic flows: Volcán de Colima, Mexico. J. Volcanol. Geotherm. Res. 179 (1–2), 157–167.